Bioorganic Chemistry 114 (2021) 105055

Contents lists available at ScienceDirect

Bioorganic Chemistry

journal homepage: www.elsevier.com/locate/bioorg

Short communication

# Biological evaluation of mitochondria targeting small molecules as potent anticancer drugs

Shuhua Luo [a], Xin Dang [a], Juntao Wang [a], Chang Yuan [a], Yixin Hu [a], Shuwen Lei [a], Yang Zhang [a], Dan Lu [a], Faqin Jiang [a], Lei Fu [a,b,*]

[a] Shanghai Key Laboratory for Molecular Engineering of Chiral Drugs, School of Pharmacy, Shanghai Jiao Tong University (SJTU), No. 800 Dongchuan Rd. Minhang District, Shanghai, 200240, PR China

[b] SJTU-Agilent Technologies Joint Laboratory for Pharmaceutical Analysis, School of Pharmacy, Shanghai Jiao Tong University (SJTU), No. 800 Dongchuan Rd. Minhang District, Shanghai, 200240, PR China

ARTICLE INFO

*Keywords:*
Mitochondria
Mitochondria-targeting compounds
ROS
Mitochondrial membrane potential
Apoptosis
Mitochondrial chemotherapy

ABSTRACT

Cancer therapy targets specific metabolic pathways or a single gene. This may result in low therapeutic effects due to drug selectivity and drug resistance. Recent studies revealed that the mitochondrial membrane potential and transmembrane permeability of cancerous mitochondria are differed from normal mitochondria. Thus, chemotherapy targeting cancerous mitochondria could be an innovative and competent strategy for cancer therapy. Previously, our work with a novel group of mitochondria targeting small molecules presented promising inhibitory capability toward various cancer cell lines and suppressed adenosine triphosphate (ATP) generation. Therefore, it is critical to understand the anticancer effect and targeting mechanism of these small molecules. This study investigated the inhibitory activity of mitochondria targeting small molecules with human cervical cancer cells – HeLa to further explore their therapeutic potential. HeLa cells were exposed to 10 μM of synthesized compounds and presented elevation in intracellular reactive oxygen species (ROS) level, impaired mitochondrial membrane potential and upregulation of apoptosis as well as necrosis. *In vivo*, HeLa cell tumor-bearing BALB/c nude mice were treated with mitochondria targeting small molecules for 12 days consecutively. Throughout this chemotherapy study, no deleterious side effects nor the appearance of toxicity was observed. Furthermore, mitochondria targeting small molecules treated groups exhibited significant down-regulation with both tumor volume and tumor weight compared to the Doxorubicin (DOX) treated group. Thus, inhibition of mitochondrial ATP synthesis, activation of intracellular ROS production, down-regulation of mitochondrial membrane potential and upregulation of apoptosis and necrosis rates are the indications of cancer therapy. In this work, we examined the anticancer capability of four mitochondria targeting small molecules *in vitro* and *in vivo*, and demonstrated a novel therapeutic approach in cancer therapy with tremendous potential.

## 1. Introduction

The mitochondrion is a highly evolved system for coordinating energy production and distribution based on available calories and oxygen. The biochemical process, known as cellular respiration, is descriptive of the metabolic reactions within the cell of organisms [1]. Cellular respiration converts biochemical energy from nutrients into ATP [2]. In addition, other vital cellular parameters are controlled by the mitochondria, including but not limited to modulation of the oxidation–reduction status [3], generation of ROS [4,5] and control of cytosolic calcium levels [6,7]. Until today, scientists have discovered that the mitochondrial genome encompasses between one to two thousand nuclear DNA (nDNA) genes, plus thousands of mitochondrial DNA (mtDNA) copies that reside within the mitochondrion [8,9]. The mutation of mtDNA could lead to various cancers, which most commonly include astrocytic tumors, colon cancer, thyroid tumors, breast tumors, head and neck tumors, and ovarian tumors, prostate and bladder cancer, neuroblastomas, and oncocytomas [8,10–14]. Moreover, mutations with mtDNA encoded for the mitochondrial enzymes have been found to associate with specific cancers [15,16]. Thus, targeting cancerous

* Corresponding author at: Shanghai Key Laboratory for Molecular Engineering of Chiral Drugs, School of Pharmacy, Shanghai Jiao Tong University (SJTU), No. 800 Dongchuan Rd. Minhang District, Shanghai, 200240, PR China.
*E-mail address:* leifu@sjtu.edu.cn (L. Fu).

https://doi.org/10.1016/j.bioorg.2021.105055
Received 11 April 2021; Received in revised form 17 May 2021; Accepted 1 June 2021
Available online 3 June 2021

mitochondria could be an efficient approach in cancer therapy. Meanwhile, one of the most challenging obstacles we confront in chemotherapy discovery today is the optimization of drug selectivity for cancerous mitochondria. Consequently, treatment with high selectivity in targeting the cancerous mitochondria is urgent [17].

Mitochondrial targeting antioxidant and anticancer compounds were first discovered during the 1990's, and these mitochondrial targeting moieties included triphenylphosphonium (TPP), rhodamine 123 and dequalinium [18–22]. The concept of mitochondria targeting was based on the membrane potential difference between cellular plasma and mitochondria [23]. Generally, plasma membrane potential ranges from −30 to −60 mV, while typical mitochondrial membrane potential reaches up to −180 mV [24]. This phenomenon facilitates positively charged molecules to have a much higher accumulation in mitochondria than cytosol. Additionally, studies have shown that cancerous mitochondrial membrane exhibited higher accessibility and transmembrane potential than normal mitochondrial membrane [19,22,25]. In the studies with rhodamine 123 (florescent lipophilic cation dye) targeting the mitochondrial matrix, rhodamine 123 was found to have markedly higher accumulation and longer retention period with cancerous mitochondria than normal mitochondria *in vitro*, and similar results were also observed with malignant cells implanted with mice models [19,25]. Additional studies with delocalized lipophilic cations, including thiopyrylium and TPP, revealed comparable results as well [26]. Together, these phenomena were used as the basis to develop mitochondria targeting antioxidant or anticancer compounds for cancer cells. Recent studies with mitochondria targeting antioxidant or anticancer compounds focused on enhancing mitochondrial accumulation, thereby improving therapeutic effects and overcoming drug resistance [23]. Meanwhile, mitochondria targeting compounds would selectively accumulate in cancerous mitochondria, constantly induce intracellular ROS generation, impair mitochondrial membrane potential and eventually lead to apoptotic cell death [27]. Thus, it is crucial to understand the signs related to mitochondria targeting compounds and their cellular effects.

Previously, our research group discovered a novel batch of mitochondria targeting small molecules that contained the TPP moiety based on Collman's work [28]. This novel group of mitochondria targeting compounds, also called the Mito-Fu family, was adapted to the thiazole warhead. Previous studies with the Mito-Fu have shown promising capability in anti-aging and anti-obesity *in vivo* [29]. In concern with the indispensable relationship between oxidative phosphorylation (OXPHOS) and tumor metabolism, further derivations were adapted to the Mito-Fu compounds focusing on the anticancer activity. Most recently, our discovery with four mitochondrial targeting small molecules presented high cytotoxicity toward cancerous cell lines (unpublished). Moreover, substantial ATP inhibition was observed with treated HeLa cells (unpublished). Thus, it is reasonable to further study the anticancer effects of these mitochondria targeting compounds both *in vitro* and *in vivo*, uncovering the underlying mechanisms.

## 2. Result and discussion

### 2.1. Chemistry

Recently within our group, 40 mitochondria targeting small molecules were synthesized and evaluated the cytotoxicity against three different cancerous cell lines – HeLa, MCF-7 and PC-3; and a non-cancerous cell line – CHO (See Appendix A). The structural design of these compounds contained three parts: the warhead, the linker and the tail group, as shown in Fig. 1. Briefly, the synthesis of these mitochondria targeting compounds shared a common tail-group - TPP, a group known to target the mitochondrion [24,30]. The warhead contained a modified thiazole derivative based on our previous findings [28,29]. Among all 40 mitochondria targeting compounds, four compounds - **R12**, **R13**, **D15** and **N2**, demonstrated high potential in cancerous-proliferation inhibition. Subsequent *in vitro* analysis confirmed that these four compounds inhibited ATP production of HeLa cells at a low concentration (See Appendix A). Therefore, further examinations were designed and performed to evaluate the anticancer capability and explore possible mechanisms of these compounds. The synthetic routes for these four compounds, **R12, R13, D15** and **N2** were illustrated in Scheme 1-3. All structures were verified by $^{1}$HNMR, $^{13}$CNMR and HRMS.

### 2.2. ROS generation analysis

Intracellular ROS elevation has been reported as a sign of early-stage apoptosis [31]. The production of intracellular ROS mainly relies upon the mitochondrion. During OXPHOS, ROS are constantly produced and released from complexes I and III on the electron transport chain in order to afford ATP production [32]. Excessive intracellular ROS can overwhelm the cellular antioxidant defense system and lead to apoptosis [27]. To determine whether **R12, R13, D15** and **N2** are capable of inducing ROS generation, 10 μM of the respective compounds were incubated with HeLa cell for 24 h and stained with fluorogenic probe – 2′,7′-Dichlorofluorescin diacetate (DCFH-DA). Intracellular ROS elevation was observed and evaluated by fluorescence microscope and flow cytometry respectively. As illustrated in Fig. 2-**a**, all 4 treated groups (**R12, R13, D15** and **N2**) and the positive control group (Ros-up) presented vigorous green fluorescence intensity, while the control group exhibited no obvious green fluorescence. By evaluating the DCFH-DA intensity (Fig. 2-**b**), intracellular ROS production of HeLa cells was increased by 1.65 (**R12**), 1.87 (**R13**), 1.44 (**D15**) and 1.95 (**N2**) fold in comparison to the control group. This phenomenon implied that these mitochondria targeting compounds might take a significant role in the early stage of HeLa cell apoptosis.

### 2.3. Mitochondrial membrane potential analysis

Mitochondrial membrane potential is one of the most essential factors during oxidative phosphorylation for ATP production. Typically, the mitochondrial membrane potential of cancer cells is displayed in the hyperpolarized state [33]. The reduced mitochondrial membrane

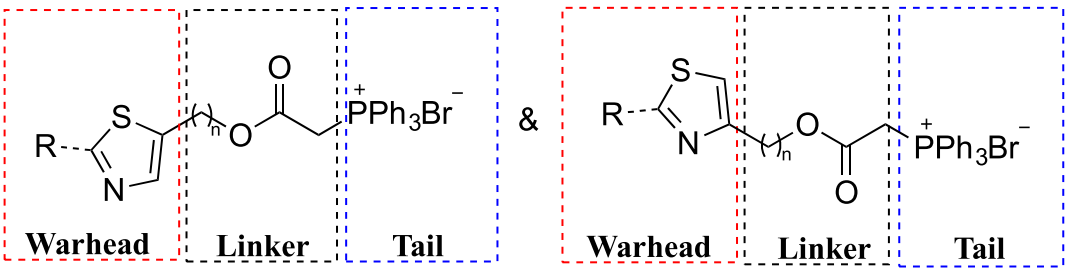


**Fig. 1.** Structural Design of the Mito-Fu Family compounds. The Mito-Fu Family compounds' basal structure contained three parts: the warhead, the linker, and the tail group.

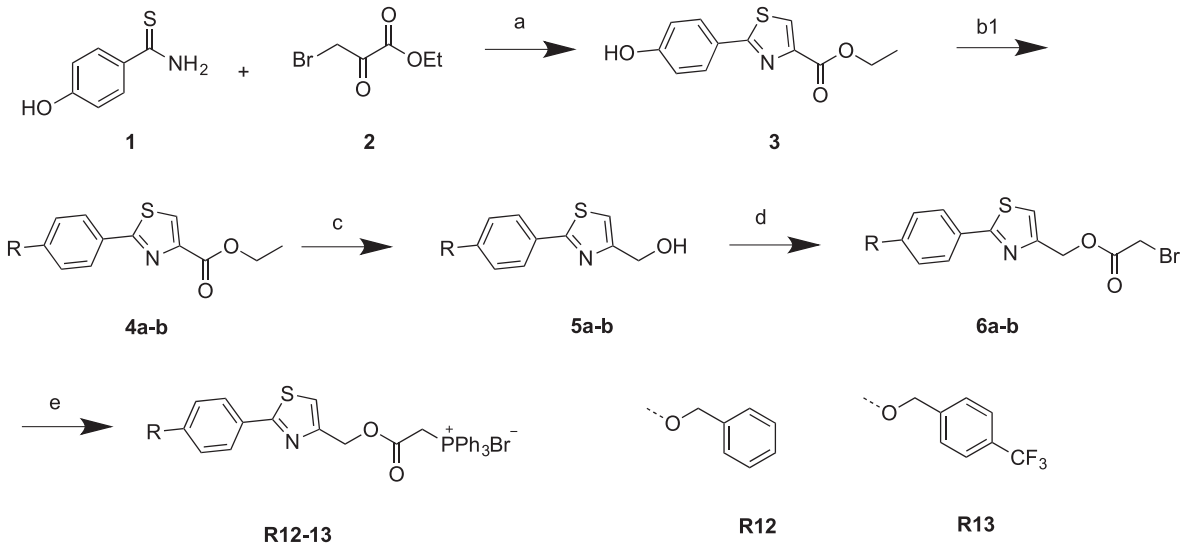


**Scheme 1.** Synthetic route for **R12-13** from 4-hydroxybenzothioamide and ethyl 3-bromo-2-chloro-3-oxopropanoate. Reagents and conditions: a: EtOH, 80 ℃ reflux, overnight; b1: (bromomethyl)benzene/1-(bromomethyl)-4-(trifluoromethyl)benzene, DMF, 80 ℃ reflux, overnight; c: $LiAlH_4$, THF, 0 ℃, 3 h; d: 2-bromoacetyl bromide, DCM, 0 ℃ to room temperature, overnight; e: $PPh_3$, toluene, room temperature, overnight.

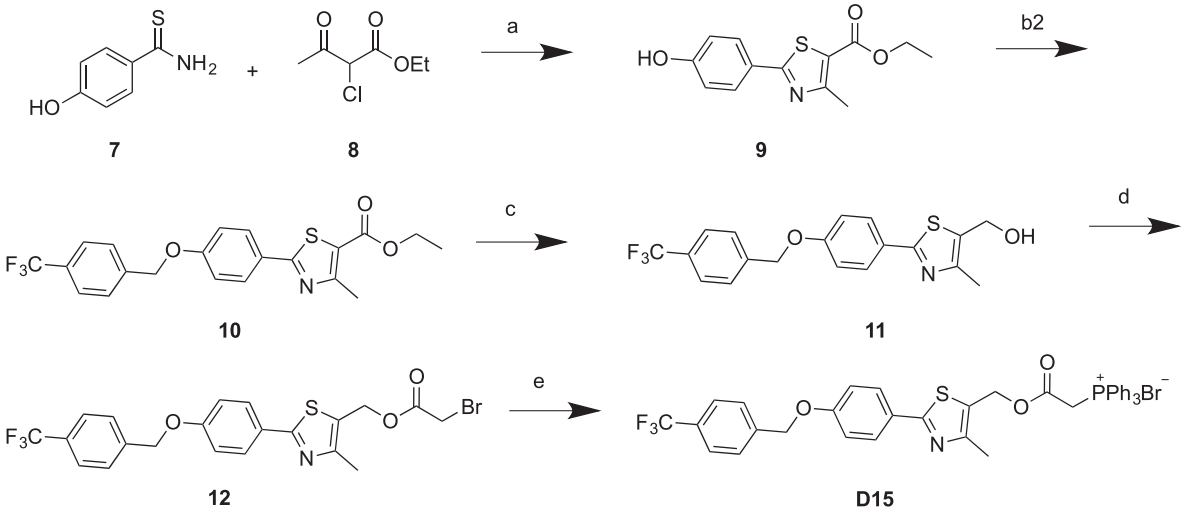


**Scheme 2.** Synthetic route for **D15** from 4-hydroxybenzothioamide and ethyl 3-bromo-2-oxopropanoate. Reagents and conditions: a: EtOH, 80 ℃ reflux, overnight; b2: 1-(bromomethyl)-4-(trifluoromethyl)benzene, $K_2CO_3$, $CH_3CN$, 80 ℃ reflux, overnight; c: $LiAlH_4$, THF, 0 ℃, 3 h; d: 2-bromoacetyl bromide, DCM, 0 ℃ to room temperature, overnight; e: $PPh_3$, toluene, room temperature, overnight.

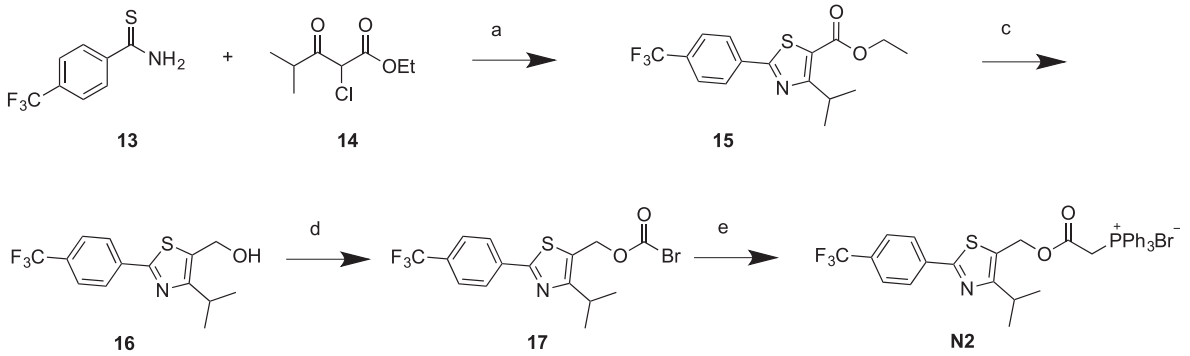


**Scheme 3.** Synthetic route for **N2** from 4-hydroxybenzothioamide and ethyl 2-chloro-4-methyl-3-oxopentanoate. Reagents and conditions: a: EtOH, 80 ℃ reflux, overnight; c: $LiAlH_4$, THF, 0 ℃, 3 h; d: 2-bromoacetyl bromide, DCM, 0 ℃ to room temperature, overnight; e: $PPh_3$, toluene, room temperature, overnight.

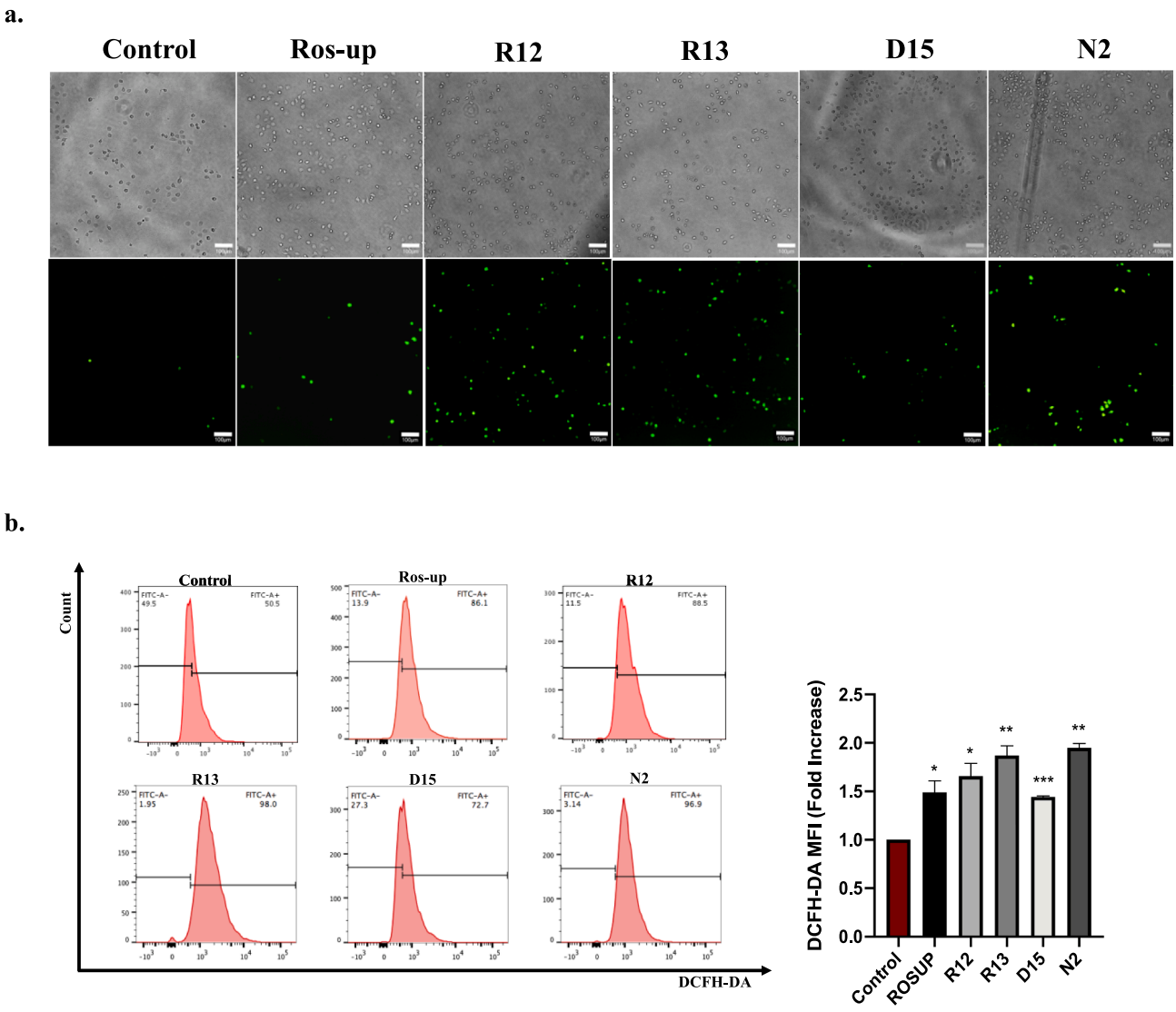


**Fig. 2.** Effects of ROS production with HeLa cells treated with mitochondria targeting compounds. Intracellular production of ROS in HeLa cells incubated with 10 μM of the indicated compound for 24 h was **(a)** observed with fluorescence microscope and **(b)** measured with flow cytometry; Ros-up was used as positive control and provided by the test kit. Three independent experiments were performed, and data was shown as mean ± SD. Asterisks indicated statistical significance compare to control using the *t*-test, (*p < 0.01; **p < 0.001; ***p < 0.0001).

potential is seen as a sign of early-stage apoptosis [34]. Furthermore, excessive production of ROS could collapse the mitochondrial membrane potential and lead to cytochrome *c* release and apoptosis machinery activation. In order to determine whether **R12, R13, D15**, and **N2** sufficiently modifies mitochondrial membrane potential, 10 μM of the respective compounds were incubated with HeLa cells for 24 h. Subsequently, HeLa cells were stained with JC-1 fluorescent probe to determine and evaluate the changes with mitochondrial membrane potential via fluorescence microscope and flow cytometry respectively. As illustrated in Fig. 3-**a**, all four treated groups (**R12, R13, D15** and **N2**) and the positive control group (CCCP) displayed substantial enhancement of green fluorescence (JC-1 monomer) intensity in comparison to the control group. This phenomenon proposed depolarization of mitochondrial membrane potential of treated HeLa cells. The fluorescence intensity of JC-1 monomers was increased by 2.55 (**R12**), 2.73 (**R13**), 1.64 (**D15**) and 2.62 (**N2**) fold in comparison to the control group, as shown in Fig. 3-**b**. In summary, these data suggested that all compounds sufficiently collapsed the mitochondrial membrane potential, and eventually led to cell death.

### 2.4. Cellular apoptosis and necrosis analysis

Apoptosis and necrosis are not only vital signs for cell survival, but they also play significant roles in cancer therapy. During apoptosis, cells undergo a programmed cell death process triggered by various chemical, physical or biological factors [35]. In contrast, necrosis is an unprogrammed cell death induced by cell injury [35]. Thus, it is crucial to examine the capability of our compounds **R12, R13, D15** and **N2** to induce cancer cell death. In order to study which type of cell death our compounds initiate, the Hoechst 33342/PI dual staining assay was performed. 10 μM of each compound was incubated with HeLa cells for 24 h, and 0.35 μM doxorubicin (DOX) was used as the positive control. Treated HeLa cells were collected and stained with Hoechst 33342/ PI stains and analyzed with flow cytometry. As shown in Fig. 4, the percentage of apoptotic cells (lower right quadrant) was increased by 6.09 (**R12**), 8.85 (**R13**), 9.50 (**D15**) and 7.88 (**N2**) fold after incubation with the respective compound. In addition, compounds **R12** and **R13** induced a 7.5-fold and 39.5-fold increase with necrotic cells (upper right quadrant) compared to the control group. These results proved that all four compounds effectively induced HeLa cell apoptosis, while compounds

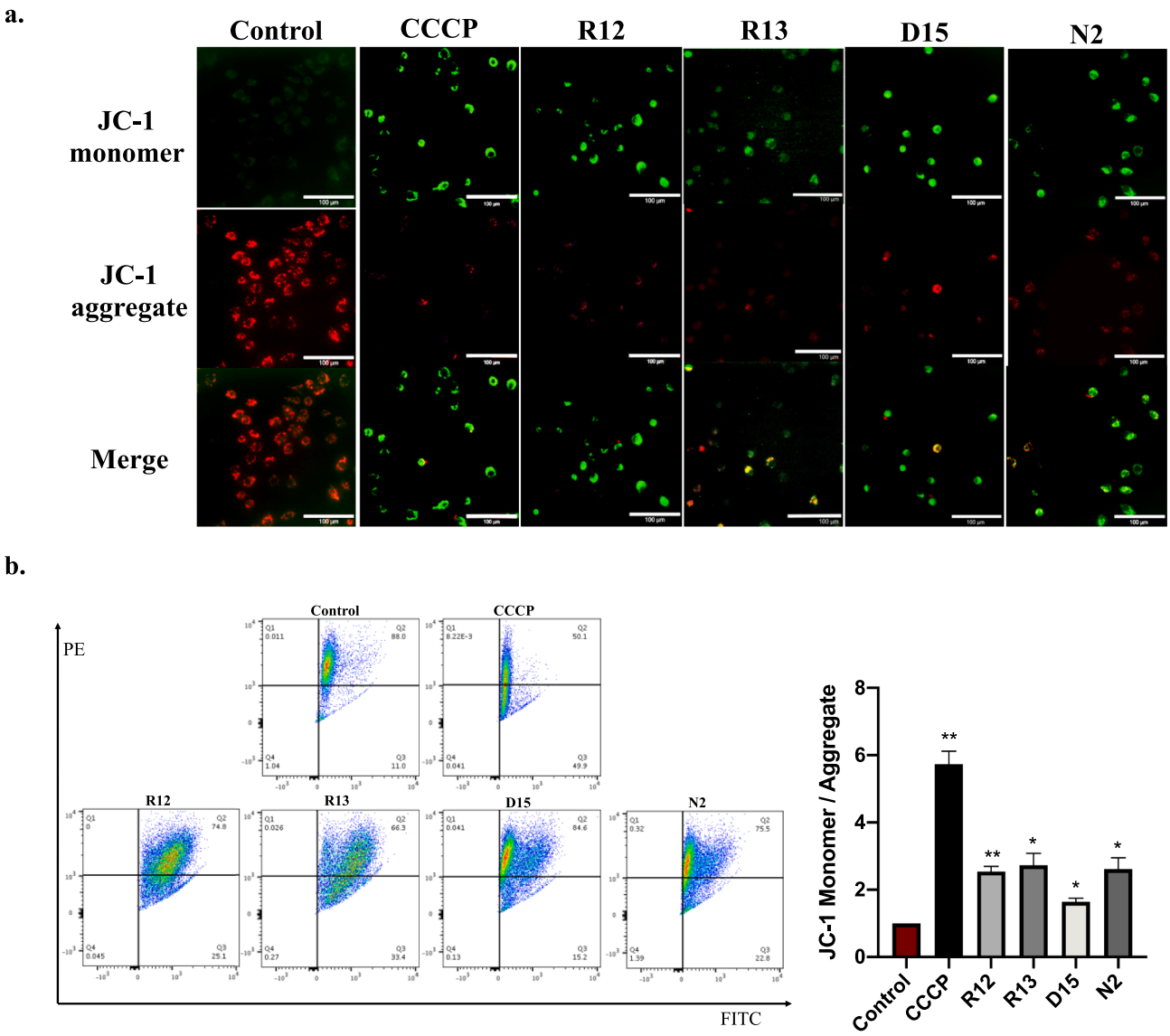


**Fig. 3.** Changes in mitochondrial membrane potential with HeLa cell treated with mitochondria targeting compounds. Changes in mitochondrial membrane potential in HeLa cells treated with 10 μM of the indicated compound for 24 h were **(a)** observed with fluorescence microscope and **(b)** evaluated with flow cytometry; 10 μM CCCP was used as positive control and incubated with HeLa cells for 30 min. Three independent experiments were performed, and data was illustrated as mean ± SD. Asterisks indicated statistical significance compared to the control using the *t*-test, (*$p < 0.02$; **$p < 0.002$).

**R12** and **R13** triggered cell necrosis.

### 2.5. Chemotherapy study

HeLa tumor cells-bearing BALB/C nude mice by subcutaneous injection of indicated compounds with different concentrations consecutively. During this *in vivo* study, tumor volume, body weight, as well as the physiological function of each animal was monitored and recorded daily. Subsequently, the final tumor was isolated and weighed for histological study. As shown in Fig. 5-**a**, treated groups demonstrated convincing inhibition in tumor growth compared to the control group during 12 days. Additionally, the body weight of all mice remained the average weight of 21 g (Fig. 5-**b**), and no death case was caused by the compounds. As tumors reached over 15 mm in diameter, nude mice were sacrificed. All collected tumors were categorized, weighed and preserved in 4% paraformaldehyde. Besides down-regulation of tumor volume, the average tumor weight was decreased in treated groups as compared to the control group. As illustrated in Fig. 4-**c**, the tumor weight of treated group demonstrated down-regulation by 40% (**R13**-10 mg/kg), 63% (**R13**-20 mg/kg), 61% (**N2**-20 mg/kg) and 79% (**N2**-50 mg/kg). Fig. 6 presented the histological slices of tumor from treated BALB/C nude mice. In comparison with the control group, both **R13**-20 mg/kg and **N2**-50 mg/kg treated group manifested the increasing tumor necrosis (black arrows) and down-regulation of the number of tumor nodes (lower row). This implied that the compounds effectively prevented tumor migration. Furthermore, **R13**-20 mg/kg shown diminished cancerous nucleolus (red arrows), indicating the restraint of cancer cell growth. These data together supported that **R13** and **N2** could repress tumor growth and transition *in vivo*.

### 2.6. Chemico-genetic Analysis: R13 and N2 induced DEGs and functional analysis

Chemico-genetic analysis of **R13** and **N2** induced differentially expressed genes (DEG) were examined and analyzed. As shown in Fig. 7a-b, volcano plots illustrated the DEG amount between **R13**, **N2** groups and their corresponding control groups. In total, 153 DEGs displayed differential expression after treatment with compound **R13**,

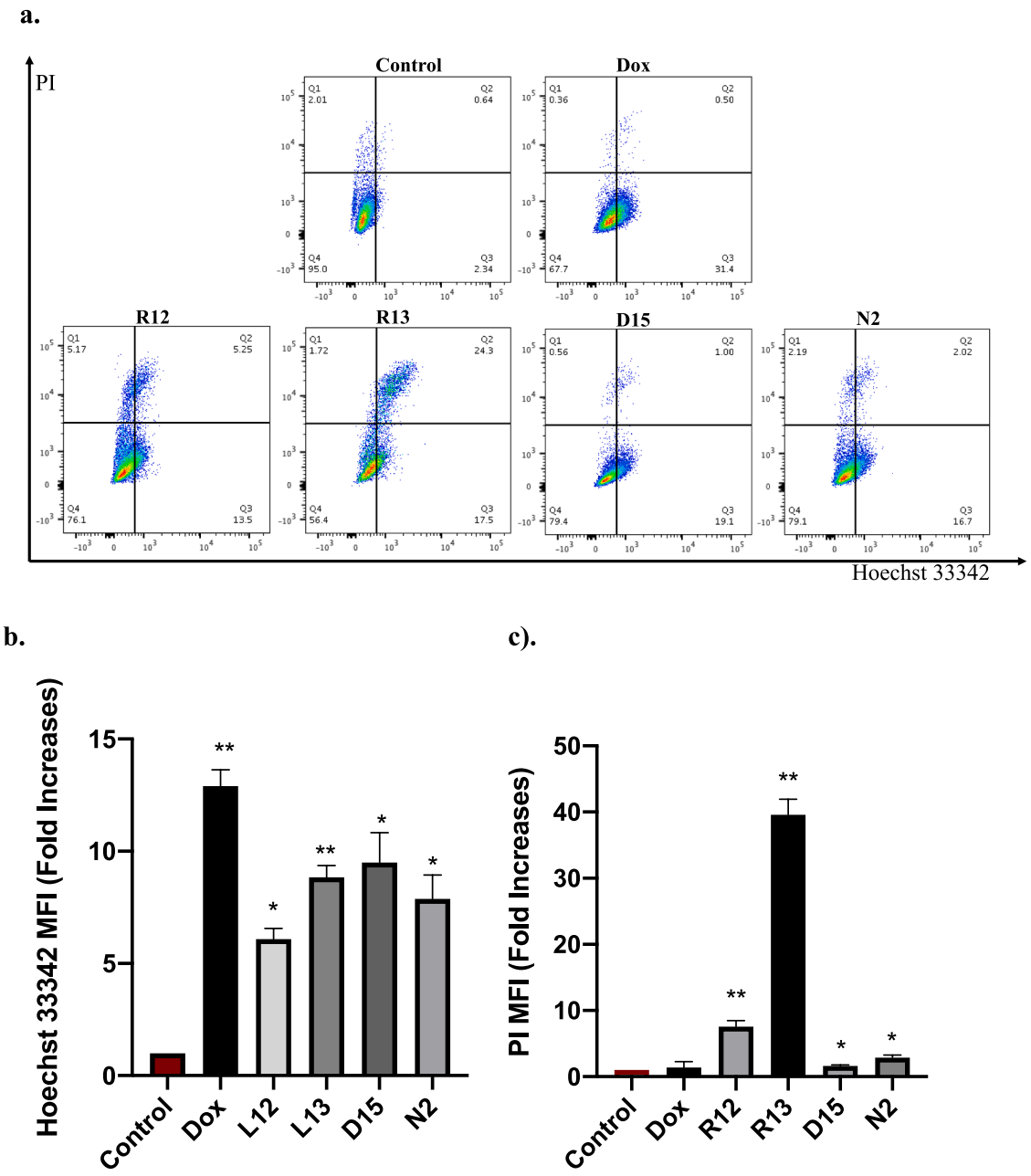


**Fig. 4.** Mitochondria targeting compounds induced cell apoptosis and necrosis. **(a)** Cell apoptosis and necrosis were analyzed using the Apoptosis and Necrosis Analysis Kit with 10 μM of the indicated compound for 24 h by flow cytometry; 0.35 μM Dox was used as positive control and incubated with HeLa cells for 24 h. Changes in **(b)** apoptosis rate and **(c)** necrosis rate of treated HeLa cells were evaluated with flow cytometry and shown in column graphs. Three independent experiments were performed, and data was shown as mean ± SD. Asterisks indicated statistical significance compared to the control using the *t*-test, (*$p < 0.01$; **$p < 0.001$).

including 86 upregulated and 67 downregulated DEGs. In **N2** treated tumor, 459 DEGs were displayed in total, in which 258 DEGs were upregulated and 201 were downregulated. The overall alteration in gene expression of DEG of **R13** and **N2** among the gene samples was visualized in Fig. 7c-d through Heatmap clustering analysis. These data confirmed gene expression changes after treatment with **R13** and **N2**. Subsequently, the Gene Ontology (GO) pathway (Fig. 7e-f) and the Kyoto encyclopedia of genes and genomes (KEGG) pathway (Fig. 7g-h) analysis was analyzed using the Database for Annotation, Visualization, and Integrated Discovery (DAVID). Both Go and KEGG pathways provided clues about the targeting mechanisms of compounds **R13** and **N2**. We found significant enrichment with GO analysis, including regulation of cell growth, regulation with membrane potential, negative regulation of nuclear division, regulation of intracellular transport, regulation of mRNA catabolic and metabolic process, regulation of apoptotic signaling pathway, epithelial cell migration and tissue migration applied to both **R13** and **N2** treated tumors. In the KEGG pathways, DEGs were enriched in cell cycle, apoptosis, RNA degradation, Wnt signaling pathway, MAPK signaling pathway and other pathways in cancer when applied to both **R13** and **N2** treated models. To be noted, the Wnt signaling pathway was marked as the sixth most enhanced pathway among 30 KEGG analytical pathways in both **R13** and **N2** treated samples.

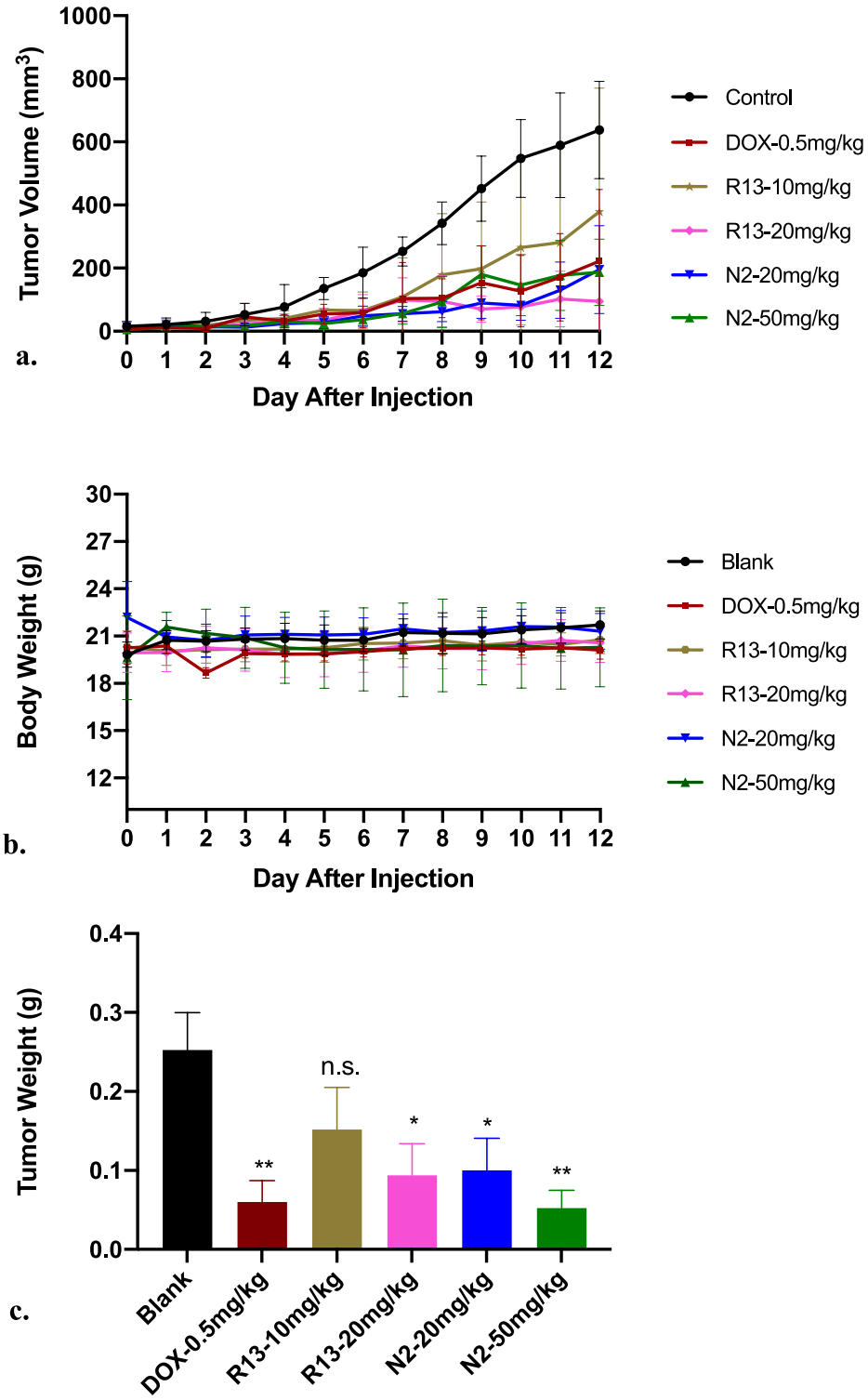


**Fig. 5.** Treatment analysis of compounds R13 and N2 on the animal subcutaneous model. **(a).** The tumor volumes of HeLa tumor-bearing nude mice treated with indicated compounds over time; tumor volumes were calculated using the ellipsoid formula = 2 × (length × width$^2$); **(b).** the body weight of each group of treated nude mice was recorded after each subcutaneous injection; **(c)** the isolated tumor-weight of each treated group after 12 days of treatment. Data was shown as mean ± SD; n = 5 for each group. Asterisks indicated statistical significance compare to control using the *t*-test, (*p < 0.1; **p < 0.01; n.s. = not significant).

### *2.7. Chemico-genetic Analysis: The Co-expression network of R13 and N2 induced DEGs*

All DEGs from the KEGG analysis were utilized as genes of interest to study the possible targeting mechanisms. Moreover, co-expression networks were built based upon the selected DEGs. The established co-expression network contained 15 nodes in both **R13** and **N2** induced DGEs models (Fig. 7k-l). Heatmap clustering analysis of respective DEGs was illustrated in Fig. 7i-j, and the expression magnitudes of DEGs were indicated with various intensities of red and blue. As shown in the **R13**-induced DEGs co-expression network, *ADCY10* demonstrated the highest correlation among all DEGs. *ADCY10* is a protein-coding gene for soluble adenylyl cyclase (sAC), and sAC is localized in the mitochondria responsible for mitochondrial cAMP production [36]. A recent study presented the role of sAC in controlling mitochondrial-dependent apoptosis, and suppression of sAC activity with selective inhibitor or knockdown of sAC with small interfering RNA simultaneously abolished mitochondrial-dependent apoptosis [37]. Therefore, we hypothesized that mitochondrial-dependent apoptosis was modulated by upregulation of *ADCY10* in this study. Within the **N2**-induced DEGs co-expression

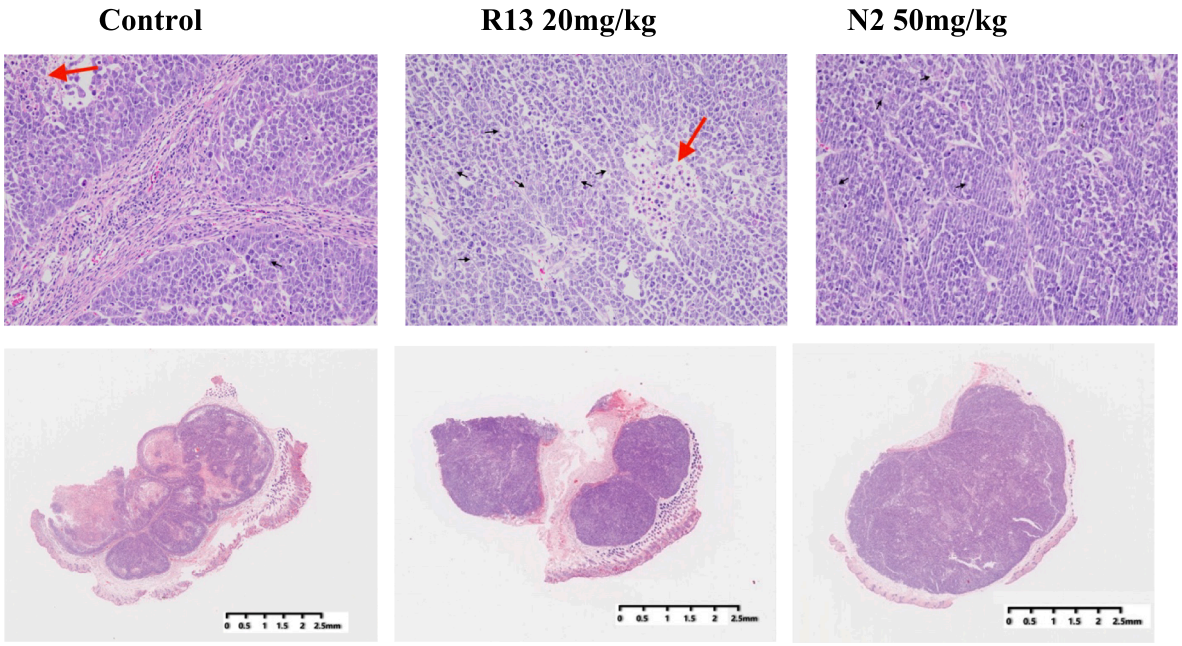


**Fig. 6.** H&E Staining of HeLa Tumors of BALB/c Mice. Tumors were presented in histological slides. **Upper row:** Red arrows indicate diminished tumor nucleolus and black arrows indicate tumor necrosis. All histology images share the same magnification of 200X. **Lower row**: The decrease in the number of tumor nodes indicated the prevention of tumor migration with treated groups compared to the control group. Tumor sizes were indicated with scale bars. (For interpretation of the references to colour in this figure legend, the reader is referred to the web version of this article.)

network, two genes, *CCNA1* and *NKD2,* manifested the highest correlation. *CCND1* is a well-known oncogene in many diseases, and this gene encodes protein Cyclin D1 which is abundant throughout the cell cycle. Accumulating studies have proven that the knockdown of *CCND1* induced glioblastoma cell apoptosis, suppressed liver cancer stem cell differentiation, regulated ovarian cancer proliferation and more [38–40]. Thus, down-regulation with *CCND1* in this study strongly confirmed the anticancer activity of **N2.** Besides *CCND1*, *NDK2* is the other most correlated DEGs in this model, and this gene encodes a protein that acts as a negative regulator of the Wnt signaling pathway. Another study has proven that overexpression of NKD2 deregulates tumor proliferation, invasion and migration ability within the osteosarcoma tumor [41]. Therefore, it is reasonable to investigate the role of *NKD2* in our study model relating to the mitochondrial targeting mechanisms in the future.

## 3. Conclusion

Previously, our group discovered 40 mitochondria-targeting compounds. Selected compounds displayed promising capability toward cancerous cell line toxicity (**R13**, $IC_{50} = 5.52$ μM), and up to 64% down-regulation with ATP generation when HeLa cells are exposed to mitochondria-targeting compound for 24 h. These results have guided us to further investigate the mechanisms and anticancer activity of the Mito-Fu family.

In this study, we confirmed the mitochondria targeting capability of four small molecules (**R12**, **R13**, **D15** and **N2**) and their ability to upregulate ROS generation, impair mitochondrial membrane potential, and induce cellular apoptosis and necrosis to various extents. Further *in vivo* study confirmed the excellent anticancer capability of **R13** and **N2** toward HeLa tumors on mice models. Consequently, chemico-genetic analysis was performed on treated tumors and disclosed the possible targeting mechanisms of these chemicals. Additionally, the down-regulation of cancer-hallmark genes such as *CCND1* strongly supported the anticancer capability of our mitochondria-targeting compounds. Beyond chemico-genetic analysis, numbers of highly correlated DEGs were extensively studied during our current research, including *ADCY10, NKD2* and a few others. Further investigations are underway to evaluate their roles not only in anticancer activity but also in mitochondria-targeting mechanisms. The discovery of anticancer capability both *in vitro* and *in vivo* supported the hypothesis of mitochondria-targeting chemotherapy in cancer. Subsequently, our research group shall focus on the underlying mechanisms in hope of moving us a step closer toward understanding the dynamic and perhaps multi-regulation of the Mito-Fu family compounds.

## 4. Experimental section

### 4.1. General information

*Chemicals.* All chemical (reagent grade) and solvents were purchased from commercial sources and purified using standard methods.

### 4.2. Experimental section

#### 4.2.1. General procedure for preparation of compounds *R12-R13*

Commercially available **1** and **2** were dissolved in anhydrous ethanol. Mixture was stirred and refluxed at 80 ℃ overnight. Upon completion, anhydrous ethanol was distilled off and extracted with minimum amount of ethyl acetate. Then intermediate **3** was extracted via recrystallization in an ice bath as a white solid. A mixture of intermediate **3** and commercially available (bromomethyl)benzene/1-(bromomethyl)-4-(trifluoromethyl)benzene was dissolved in dimethylformamide and refluxed at 80 ℃ overnight. The reaction was quenched by $H_2O$ and extracted by ethyl acetate. The mixture of ethyl acetate solutions was dried and evaporated, and intermediate **4a-b** were afforded by silica chromatography as white solids. Then intermediates **4a-b** were dissolved in tetrahydrofuran, and $LiAlH_4$ was added to solution dropwise under the ice bath. Reaction mixture was stirred at room temperature for 3 h. Then reaction was quenched with $H_2O$ dropwise under ice-bath and extracted by ethyl acetate. Collected ethyl acetate solutions were dried and evaporated. Silica chromatography was performed to afford intermediate **5a-b** as yellow solids. A solution of **5a-b** dissolved in dichloromethane was added with 2-bromoacetyl bromide

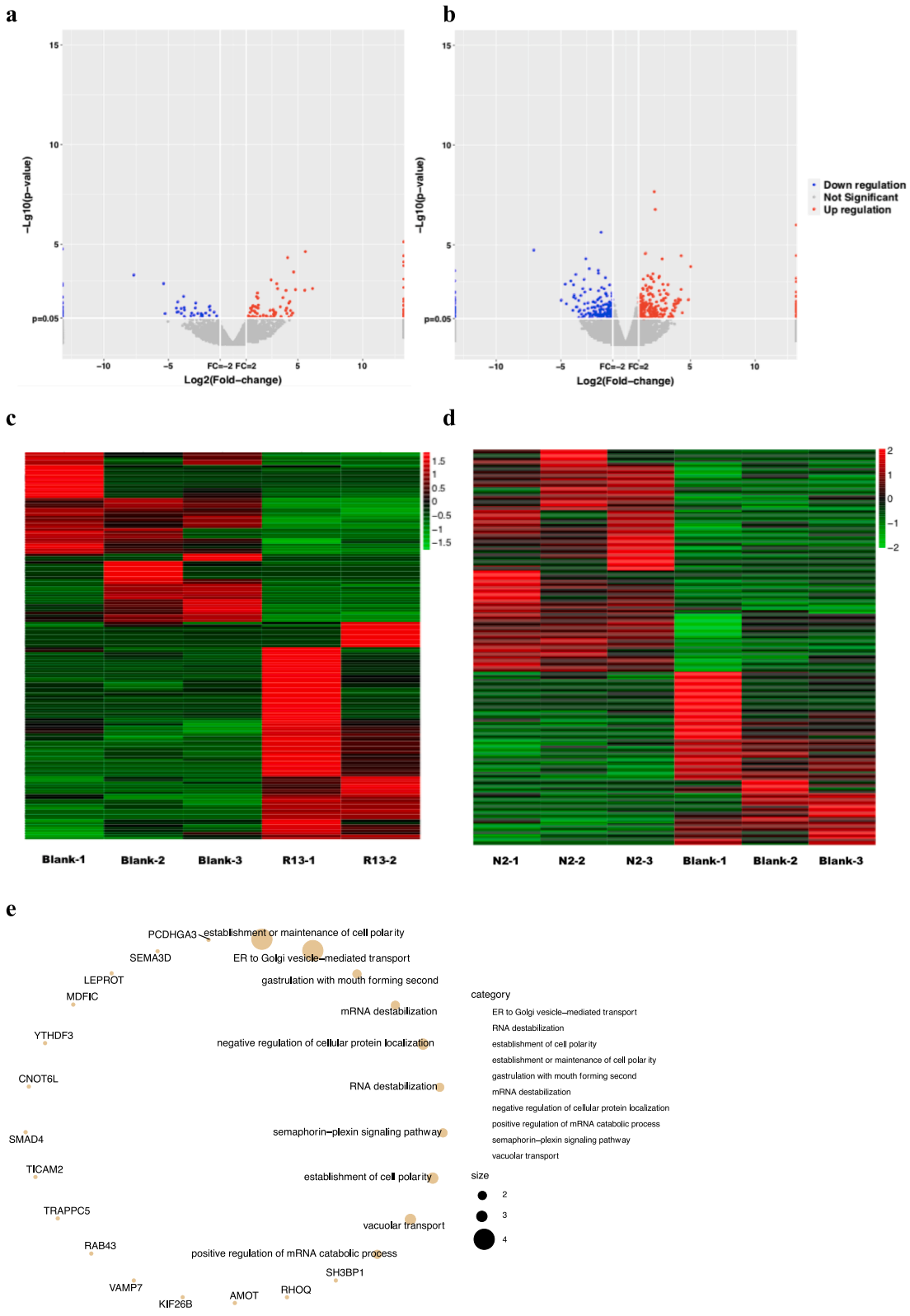


**Fig. 7.** R13 and N2 Induced Gene Expression Changes in HeLa Tumor Bearing Mice. The volcano plots of R13 **(a)** and N2 **(b)** induced gene expression changes based on all genes detected by the microarray; The heatmap of R13 **(c)** and N2 **(d)** induced DEGs are illustrated; DEG fold change $\geq$ 2.0. GO pathway analysis of R13 **(e)** and N2 **(f)** induced DEGs, 10 most enrich biological processes were selected in each model; KEGG pathway analysis of R13 **(g)** and N2 **(h)** induced DEGs, 10 most enrich biological processes were selected in each model; The heatmaps of R13 **(i)** and N2 **(j)** induced DEGs from the respective KEGG pathways; R13-induced DEGs co-expression network **(k)** and N2-induced DEGs co-expression network **(l)**, red circles represented upregulation of gene expression and blue circles represented down-regulation of gene expression determined by the log (fold change) with each model; the size of each circle corresponding to the correlation degree, and the larger the circle represents a higher correlation degree and vice versa. (For interpretation of the references to colour in this figure legend, the reader is referred to the web version of this article.)

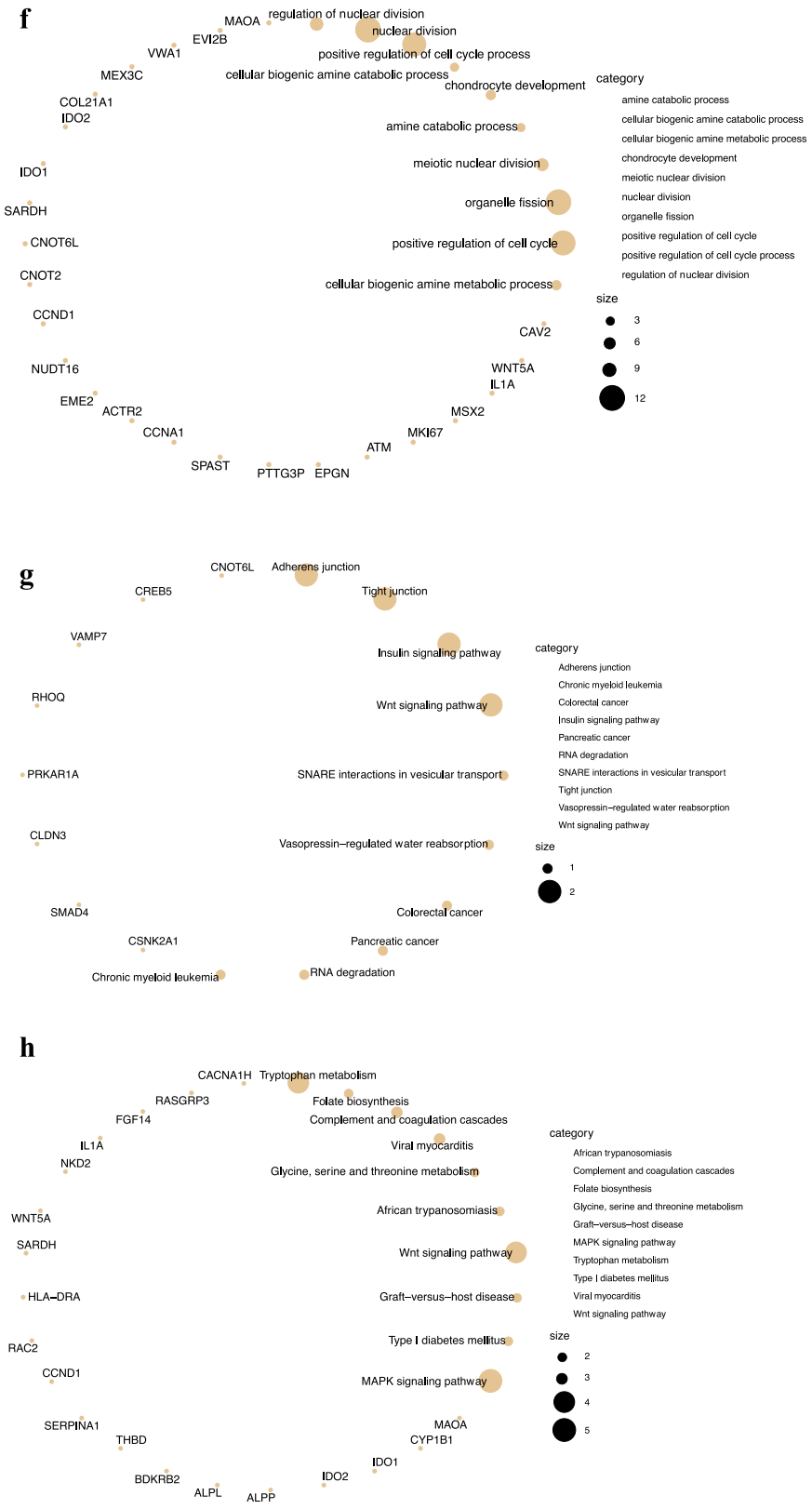


**Fig. 7.** (*continued*).

dropwise under an ice bath. Reaction mixture was stirred at room temperature overnight and reaction was monitored via TLC. Then, reaction mixture was washed with saturated $NaHCO_3$, and organic layers were collected, dried, and evaporate. Silica chromatography was performed to afford intermediates **6a-b** as white solids. Finally, intermediates **6a-b** dissolved in toluene were added with $PPh_3$. Reaction mixture was stirred at room temperature overnight and monitored with TLC. Upon completion, the precipitate was collected and washed with toluene to provide **R12 & R13** as white solids.

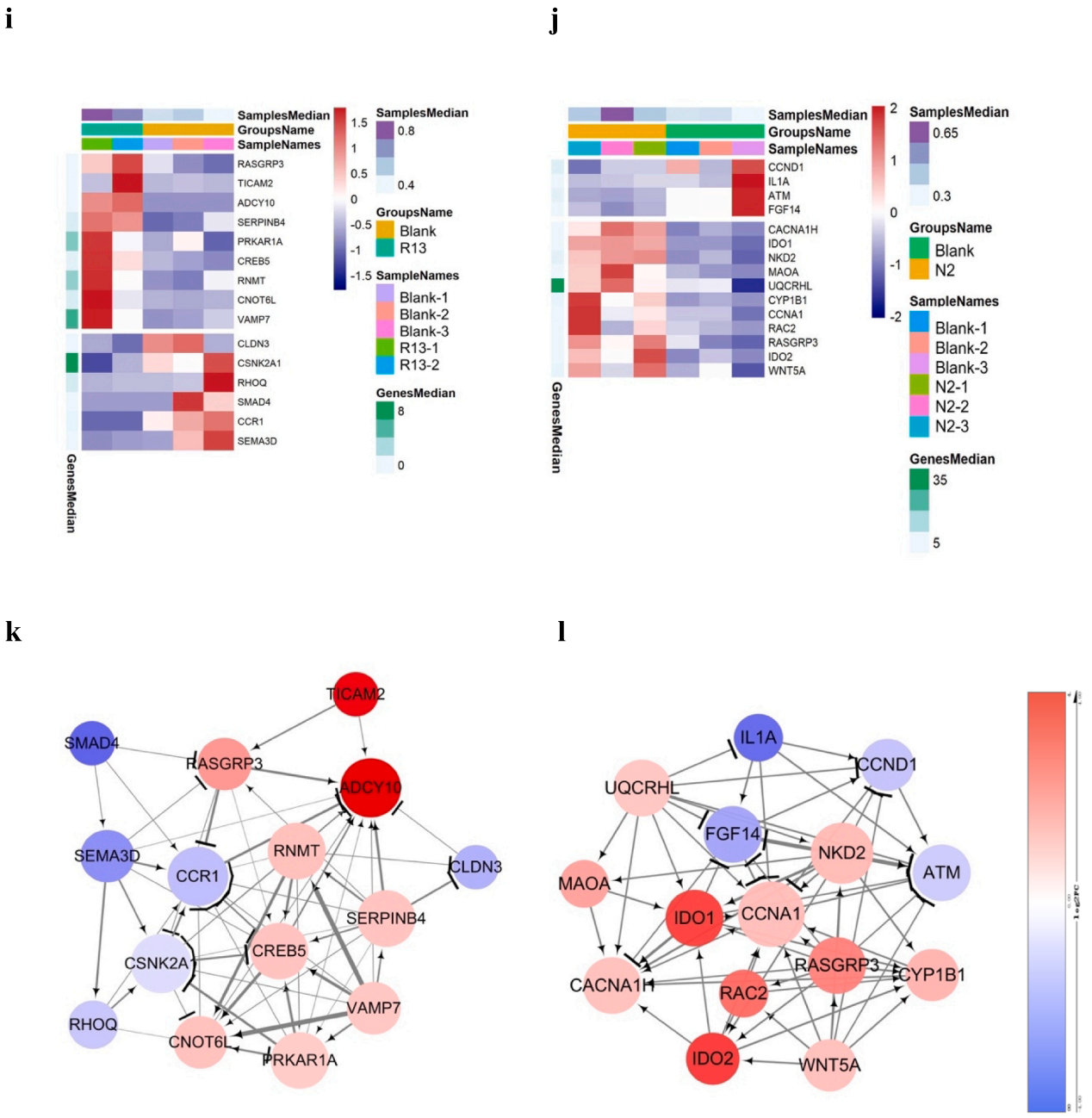


**Fig. 7.** (*continued*).

*4.2.1.1. (2-((2-(4-(benzyloxy)phenyl)thiazol-4-yl)methoxy)-2-oxoethyl) triphenylphosphonium bromide **(R12)***. White solid, yield 75%. $^{1}$H NMR (400 MHz, DMSO-$d_6$) $\delta$ 7.87 – 7.74 (m, 11*H*), 7.70 (td, $J$ = 7.7, 3.7 Hz, 6H), 7.57 (s, 1H), 7.50 – 7.47 (m, 2H), 7.45 – 7.39 (m, 2H), 7.37 – 7.32 (m, 1H), 7.18 – 7.12 (m, 2H), 5.46 (d, $J$ = 14.6 Hz, 2H), 5.20 (s, 4H). $^{13}$C NMR (101 MHz, Chloroform-d) $\delta$ 155.15, 141.85, 140.21, 138.92, 138.82, 135.24, 135.11, 133.66, 132.95, 120.64, 45.39, 45.18, 44.97, 44.76, 44.55, 44.34, 44.13. HRMS(ESI) *m/z* $C_{37}H_{31}BrNO_3PS$ calcd. for $[M]^+$ 600.1757, found: 600.1757

*4.2.1.2. (2-oxo-2-((2-(4-((4-(trifluoromethyl)benzyl)oxy)phenyl)thiazol-4-yl)methoxy)ethyl)triphenylphosphonium bromide **(R13)***. White solid, yield 93%. $^{1}$H NMR (400 MHz, DMSO-$d_6$) $\delta$ 7.90 – 7.76 (m, 13H), 7.70 (td, $J$ = 7.8, 3.3 Hz, 8H), 7.60 (s, 1H), 7.18 (d, $J$ = 8.5 Hz, 2H), 5.50 (d, $J$ = 14.6 Hz, 2H), 5.34 (s, 2H), 5.21 (s, 2H). $^{13}$C NMR (101 MHz, DMSO-$d_6$) $\delta$ 167.83, 160.22, 150.43, 142.01, 135.47, 135.44, 134.18, 134.07, 130.49, 130.36, 128.52, 128.23, 126.36, 125.81, 125.77, 119.72, 118.92, 118.04, 115.94, 69.01, 63.33, 30.17. HRMS(ESI) *m/z* $C_{38}H_{30}BrF_3NO_3PS$ calcd for $[M]^+$ 668.1631, found: 668.1611

*4.2.2. General procedure for preparation of compounds **D15***

Commercially available **7** and **8** were dissolved in anhydrous ethanol. Mixture was stirred and refluxed at 80 ℃ overnight. Upon completion, anhydrous ethanol was distilled off and extracted with minimum amount of ethyl acetate. Then intermediate **9** was extracted via recrystallization in an ice bath as a white solid. A mixture of intermediate **9** and commercially available 1-(bromomethyl)-4-(trifluoromethyl)benzene was dissolved in acetonitrile with potassium carbonate and refluxed at 80 ℃ overnight. The reaction was quenched by $H_2O$ and extracted by ethyl acetate. The mixture of ethyl acetate solutions was dried and evaporated, and intermediate **10** was afforded by silica chromatography as white solids. Then intermediate **10** was

dissolved in tetrahydrofuran, and $LiAlH_4$ was added to solution dropwise under ice-bath. Reaction mixture was stirred at room temperature for 3 h. Then reaction was quenched with $H_2O$ dropwise under ice-bath and extracted by ethyl acetate. Collected ethyl acetate solutions were dried and evaporated. Silica chromatography was performed to afford intermediate **11** as yellow solids. A solution of **11** dissolved in dichloromethane was added with 2-bromoacetyl bromide dropwise under ice-bath. Reaction mixture was stirred at room temperature overnight and reaction was monitored via TLC. Then, reaction mixture was washed with saturated $NaHCO_3$, and organic layers were collected, dried, and evaporate. Silica chromatography was performed to afford intermediate **12** as white solid. Finally, intermediates **12** dissolved in toluene were added with $PPh_3$. Reaction mixture was stirred at room temperature overnight and monitored with TLC. Upon completion, precipitate was collected and washed with toluene to provide **D15** as white solids.

*4.2.2.1. (2-((4-methyl-2-(4-((4-(trifluoromethyl)benzyl)oxy)phenyl)thiazol-5-yl)methoxy)-2-oxoethyl)triphenylphosphonium bromide **(D15)**.* White solid, yield 71%.$^1$H NMR (400 MHz, DMSO-$d_6$) $\delta$ 7.86 – 7.69 (m, 23H), 5.40 (d, $J$ = 14.7 Hz, 2H), 5.32 (d, $J$ = 3.9 Hz, 4H), 2.25 (s, 3H). $^{13}$C NMR (101 MHz, DMSO-$d_6$) $\delta$166.63,164.90, 160.29,153.75, 135.57, 135.50, 135.47, 134.15, 134.04, 130.55, 130.42, 128.51, 128.07, 126.38, 126.01, 125.85, 125.81, 125.74, 123.78, 118.89, 118.00, 115.97, 68.98, 59.53, 40.41, 40.20, 29.99, 15.26. HRMS(ESI) *m/z* $C_{39}H_{32}F_3NO_3PS$, calcd for $[M + H]^+$ 683.1865, found: 683.1833

*4.2.3. General procedure for preparation of compounds **N2***

Commercially available **13** and **14** were dissolved in anhydrous ethanol. Mixture was stirred and refluxed at 80 ℃ overnight. Upon completion, anhydrous ethanol was distilled off and extracted with minimum amount of ethyl acetate. Then intermediate **15** was extracted via recrystallization in an ice bath as a white solid. Then intermediates **15** was dissolved in tetrahydrofuran, and $LiAlH_4$ was added to solution dropwise under ice-bath. Reaction mixture was stirred at room temperature for 3 h. Then reaction was quenched with $H_2O$ dropwise under ice-bath and extracted by ethyl acetate. Collected ethyl acetate solutions were dried and evaporated. Silica chromatography was performed to afford intermediate **16** as yellow solids. A solution of **16** dissolved in dichloromethane was added with 2-bromoacetyl bromide dropwise under ice-bath. Reaction mixture was stirred at room temperature overnight and reaction was monitored via TLC. Then, reaction mixture was washed with saturated $NaHCO_3$, and organic layers were collected, dried, and evaporate. Silica chromatography was performed to afford intermediate **17** as white solid. Finally, intermediates **17** dissolved in toluene were added with $PPh_3$. Reaction mixture was stirred at room temperature overnight and monitored with TLC. Upon completion, the precipitate was collected and washed with toluene to provide **N2** as white solids.

*4.2.3.1. (2-((4-isopropyl-2-(4-(trifluoromethyl)phenyl)thiazol-5-yl) methoxy)-2-oxoethyl)triphenylphosphonium bromide **(N2)**.* White solid, yield 66%. $^1$H NMR (400 MHz, DMSO-$d_6$) $\delta$ 7.91 – 7.69 (m, 19H), 5.45 (d, $J$ = 14.6 Hz, 2H), 5.41 (s, 2H), 3.17 (dt, $J$ = 13.6, 6.9 Hz, 1H), 1.18 (d, $J$ = 6.8 Hz, 6H). $^{13}$C NMR (101 MHz, DMSO-$d_6$) $\delta$ 165.35, 164.99, 163.60, 136.75, 135.51, 135.48, 134.17, 134.06,133.74, 130.60, 130.55, 130.47, 130.42, 127.15, 126.79, 126.75, 125.20, 118.89, 118.00, 58.88, 30.02, 27.98, 23.03. HRMS(ESI) *m/z* $C_{34}H_{30}F_3NO_2PS$, calcd for $[M]^+$ 604.1681, found: 604.1668

### 4.3. Cell culture and maintenance

All HeLa cells used in this study were purchased from China Life Science College (Shanghai, PRC). DMEM culture medium, Phosphate Buffered Saline (PBS) and 100X Penicillin/Streptomycin Solution were purchased from HyClone. Fetal Bovine Serum (FBS), Trypsin-EDTA (2.5%) and Phenol red were purchased from UBI. HeLa cell line was grown in the supplementation of 10% FBS and 1% 100X Penicillin/Streptomycin Solution in a humidified atmosphere of 5% $CO_2$ at 37 °C.

### 4.4. ROS assay

HeLa cells were grown at a density of 5 × $10^5$ cells/mL in a 6-well plate and treated with compounds R12, R13, D15 and N2 at a concentration of 10 μM for 24 h with proper culture medium in 5% $CO_2$ at 37 °C. For fluorescent microscope observation, treated HeLa cells were washed twice with PBS and stained with 10 mM DCFH-Da dissolved in DMEM and incubated at 37 °C in the dark for 20 min. Then, DCFH-Da stained cells were washed twice with ice-cold PBS and fluorescent microscope observation was performed at the proper excitation wavelength (488 nm) and emission wavelength (525 nm). For flow cytometry evaluation, treated cells were washed twice with PBS and collected at 1500 rpm. Then, treated cells were resuspended in 10 mM DCFH-DA that dissolved in DMEM and incubated at 37 °C in the dark for 20 min. Subsequently, DCFH-Da stained cells were collected, washed twice with ice-cold PBS and resuspended in DMEM. Intracellular ROS concentration was evaluated with flow cytometry at the proper excitation wavelength (488 nm) and emission wavelength (525 nm).

### 4.5. Mitochondrial membrane potential assay

HeLa cells were grown at a density of 5 × $10^5$ cells/ml in a 6-well plate and treated with compounds R12, R13, D15 and N2 at a concentration of 10 μM for 24 h with proper culture medium in 5% $CO_2$ at 37 °C. For fluorescent microscope observation, treated HeLa cells were washed with PBS and stained with JC-1 staining solution and incubated at 37 °C in the dark for 20 min. Then, stained cells were washed with ice-cold JC-1 Buffer. JC-1 monomers were observed by fluorescent microscope at an excitation of 490 nm and emission of 530 nm. For flow cytometry evaluation, treated cells were collected at 1500 rpm and stained with JC-1 staining solution and incubated at 37 °C in the dark for 20 min. Subsequently, cells were rinsed with JC-1 buffer and resuspended in JC-1 Buffer. Loss of mitochondrial membrane potential was determined with flow cytometry by evaluating the relative JC-1monomer and aggregate ratio.

### 4.6. Apoptosis and necrosis assay

Hoechst 33342 and PI dual staining were used for apoptosis and necrosis analysis. HeLa cells were grown at a density of 5 × $10^5$ cells/ml in a 6-well plate and treated with compounds R12, R13, D15 and N2 at a concentration of 10 μM for 24 h with proper culture medium in 5% $CO_2$ at 37 °C. Then HeLa cells were collected at 1500 rpm and resuspended in the staining buffer. Subsequently, Hoechst/PI probes were resuspended with treated cells and incubated at 0 °C for 20 min. Samples were analyzed with flow cytometry and data was analyzed with FlowJo software.

### 4.7. Chemotherapy study – Tumor model and treatment

All animal experimental procedures were approved by Shanghai Jiao Tong University's review board and administrative panel on laboratory animal according to national guidelines (Ethic Number: 20201127–01). Animals used for this research project include female BALB/c mice (Shanghai SLAC Laboratory Animal Co. Ltd). A total of 45 female BALB/c mice were group-housed in a pathogen-free facility with 21 °C and 12 h light/12 h dark cycle, with full access to water and standard laboratory food.

In order to build the tumor model, HeLa cells with concentration of 1 × $10^6$ cells /100 μL in serum-free DMEM were inoculated subcutaneously in the lower right thigh of each nude mouse. When the diameter of

the tumor reached 4–5 mm, nude mice were randomly divided into six groups and labeled. Group I – the control group and treatment with 100 μL saline solution; Group II – the positive control group and treatment with 0.5 mg/kg DOX; Group III – treatment with 20 mg/kg N2 compound; Group IV – treatment with 50 mg/kg N2 compound; Group V – treatment with 10 mg/kg R13 compound; Group VI – treatment with 20 mg/kg R13 compound. All compounds were dissolved in saline (contain 0.1% DMSO) and 100 μL of each solution were administrated subcutaneously to nude mice. This experiment was carried out consecutively from day 0 to day 11. Meanwhile, the width and length of ellipsoid tumors, as well as weights, were measured and recorded after each subcutaneous administration (from day 0 to 12). On day 12, nude mice were sacrificed. Tumors, kidneys and livers were isolated and preserved for future analysis.

### 4.8. Hematoxylin-eosin (H&E) staining

Tumor tissues collected from BALB/c nude mice were preserved in 4% paraformaldehyde and stained with H&E staining according to the manual H&E Staining protocol [42]. Sectioned tissues were observed and photographed under 200X and 400X microscope.

### 4.9. Microarray analysis

Total mRNA from R13-20 mg/kg, N2-50 mg/kg and saline-treated tumors were extracted using the Trizol Reagent (Invitrogen) and miRNA isolation kit (Ambion, Austin, TX, USA) according to the commercial protocol. RNA yield was determined by NanoDrop spectrophotometer (Thermo Scientific, USA). Then RNA integrity was evaluated with agarose gel electrophoresis and ethidium bromide. The Agilent Gene Expression Kit was used, and double-stranded cDNA was transcribed from total RNA, then synthesized into cDNA with Cyanine-3-CTP labels to hybridized with the microarray. After washing, microarray was scanned with Agilent Scanner G2505C, and Feature Extraction Software (version 10.7.1.1, Agilent) was used to analyze the array images. Genespring was used for raw data analysis, and raw data was normalized with quantile algorithm to detect the differential genes. DEGs were calculated as the gene with fold changes $\geq 2.0$ and $p$-value $< 0.05$.

### 4.10. GO and KEGG pathways analysis

Both GO and KEGG pathway analyses were performed using the DAVID system. The adjusted data function from the R package *gplots* was used to transformed data into Log2 and medium centered style. Heatmap clustering analysis was also performed with R package *average linkage*. Using the DAVID system, assigned genes were introduced and GO biological pathways and KEGG molecular pathways were analyzed. GO biological pathways were identified related to the EASE score, $p$-value $< 0.01$, while KEGG molecules pathways were identified related to the EASE score, $p$-value $< 0.05$. The importunateness of pathways relied on the higher enrichment with specific genes and gene count.

### 4.11. Correlation and Co-expression analysis

The gene-gene interaction network was established based the Pearson's correlation coefficient, and Cytoscape 3.6.1 software was used to construct the gene-gene co-expression network.

### 4.12. Statistical analysis

All statistical analysis was performed by GraphPad, Prims 8 Version 8.2.1. All *in vitro* experiments were replicated at least thrice, and similar results were yielded and analyzed for each experiment.

## Declaration of Competing Interest

The authors declare that they have no known competing financial interests or personal relationships that could have appeared to influence the work reported in this paper.

## Acknowledgements

This research was supported by the Chinese government scholarship (CSC for SH Luo), Medical-Engineering Joint Fund of Shanghai Jiao Tong University (No. YG2017MS29, No. ZH2018ZDB07), and Agilent research Award (Agilent Grant ID #4608). The authors would like to also thank Tony Zhang for his careful language proofreading and corrections.

## Appendix A. Supplementary data

Supplementary data to this article can be found online at https://doi.org/10.1016/j.bioorg.2021.105055.

## References

[1] M. Ristow, T.J. Schulz, Warburg and his Legacy, 2009.
[2] D.C. Wallace, Why do we still have a maternally inherited mitochondrial DNA? Insights from evolutionary medicine, Annual review of biochemistry 76 (2007) 781–821.
[3] D. Anastasiou, G. Poulogiannis, J.M. Asara, M.B. Boxer, J.K. Jiang, M. Shen, G. Bellinger, A.T. Sasaki, J.W. Locasale, D.S. Auld, C.J. Thomas, M.G. Vander Heiden, L.C. Cantley, Inhibition of pyruvate kinase M2 by reactive oxygen species contributes to cellular antioxidant responses, Science 334 (6060) (2011) 1278–1283.
[4] D.C. Wallace, W. Fan, V. Procaccio, Mitochondrial energetics and therapeutics, Annual review of pathology 5 (2010) 297–348.
[5] R.H. Burdon, Superoxide and hydrogen peroxide in relation to mammalian cell proliferation, Free Radical Biology and Medicine 18 (4) (1995) 775–794.
[6] J.G. McCormack, R.M. Denton, A comparative study of the regulation of Ca2+ of the activities of the 2-oxoglutarate dehydrogenase complex and NAD+-isocitrate dehydrogenase from a variety of sources, The Biochemical journal 196 (2) (1981) 619–624.
[7] J.G. McCormack, A.P. Halestrap, R.M. Denton, Role of calcium ions in regulation of mammalian intramitochondrial metabolism, Physiological reviews 70 (2) (1990) 391–425.
[8] J.Y. Guo, H.-Y. Chen, R. Mathew, J. Fan, A.M. Strohecker, G. Karsli-Uzunbas, J.J. Kamphorst, G. Chen, J.M.S. Lemons, V.J.G. Karantza, Development, Activated Ras requires autophagy to maintain oxidative metabolism and tumorigenesis, 25(5) 460-470.
[9] D.C. Wallace, Mitochondrial genetic medicine, Nature genetics 50 (12) (2018) 1642–1649.
[10] T.M. Horton, J.A. Petros, A. Heddi, J. Shoffner, A.E. Kaufman, S.D. Graham Jr., T. Gramlich, D.C. Wallace, Novel mitochondrial DNA deletion found in a renal cell carcinoma, Genes, chromosomes & cancer 15 (2) (1996) 95–101.
[11] P.F. Chinnery, D.C. Samuels, J. Elson, D.M. Turnbull, Accumulation of mitochondrial DNA mutations in ageing, cancer, and mitochondrial disease: is there a common mechanism? Lancet (London, England) 360 (9342) (2002) 1323–1325.
[12] W.C. Copeland, J.T. Wachsman, F.M. Johnson, J.S. Penta, Mitochondrial DNA alterations in cancer, Cancer investigation 20 (4) (2002) 557–569.
[13] G. Gasparre, E. Hervouet, E. de Laplanche, J. Demont, L.F. Pennisi, M. Colombel, F. Mège-Lechevallier, J.Y. Scoazec, E. Bonora, R. Smeets, J. Smeitink, V. Lazar, J. Lespinasse, S. Giraud, C. Godinot, G. Romeo, H. Simonnet, Clonal expansion of mutated mitochondrial DNA is associated with tumor formation and complex I deficiency in the benign renal oncocytoma, Human molecular genetics 17 (7) (2008) 986–995.
[14] A. Bartoletti-Stella, N.C. Salfi, C. Ceccarelli, M. Attimonelli, G. Romeo, G. Gasparre, Mitochondrial DNA mutations in oncocytic adnexal lacrimal glands of the conjunctiva, Archives of ophthalmology (Chicago, Ill. : 1960) 129(5) (2011) 664-6.
[15] C. Bardella, P.J. Pollard, I. Tomlinson, SDH mutations in cancer, Biochim Biophys Acta 1807 (11) (2011) 1432–1443.
[16] L. Dang, D.W. White, S. Gross, B.D. Bennett, M.A. Bittinger, E.M. Driggers, V. R. Fantin, H.G. Jang, S. Jin, M.C. Keenan, K.M. Marks, R.M. Prins, P.S. Ward, K. E. Yen, L.M. Liau, J.D. Rabinowitz, L.C. Cantley, C.B. Thompson, M.G. Vander Heiden, S.M. Su, Cancer-associated IDH1 mutations produce 2-hydroxyglutarate, Nature 462 (7274) (2009) 739–744.
[17] J. Ma, L. Li, K. Yue, Y. Li, H. Liu, P.G. Wang, C. Wang, J. Wang, W. Luo, S. Xie, Bromocoumarinplatin, targeting simultaneously mitochondria and nuclei with p53 apoptosis pathway to overcome cisplatin resistance, Bioorg Chem 99 (2020), 103768.
[18] L. Ernster, G. Schatz, Mitochondria: a historical review, The Journal of cell biology 91 (3 Pt 2) (1981) 227s–255s.

[19] T.J. Lampidis, Y. Hasin, M.J. Weiss, L.B. Chen, Selective killing of carcinoma cells "in vitro" by lipophilic-cationic compounds: a cellular basis, Biomedicine & pharmacotherapy = Biomedecine & pharmacotherapie 39 (5) (1985) 220–226.
[20] M.J. Weiss, J.R. Wong, C.S. Ha, R. Bleday, R.R. Salem, G.D. Steele Jr., L.B. Chen, Dequalinium, a topical antimicrobial agent, displays anticarcinoma activity based on selective mitochondrial accumulation, Proceedings of the National Academy of Sciences of the United States of America 84 (15) (1987) 5444–5448.
[21] J.E. Christman, D.S. Miller, P. Coward, L.H. Smith, N.N. Teng, Study of the selective cytotoxic properties of cationic, lipophilic mitochondrial-specific compounds in gynecologic malignancies, Gynecologic oncology 39 (1) (1990) 72–79.
[22] S.H. Dairkee, A.J. Hackett, Differential retention of rhodamine 123 by breast carcinoma and normal human mammary tissue, Breast cancer research and treatment 18 (1) (1991) 57–61.
[23] G. Battogtokh, Y.Y. Cho, J.Y. Lee, H.S. Lee, H.C. Kang, Mitochondrial-Targeting Anticancer Agent Conjugates and Nanocarrier Systems for Cancer Treatment, Front Pharmacol 9 (2018) 922.
[24] J. Zielonka, J. Joseph, A. Sikora, M. Hardy, O. Ouari, J. Vasquez-Vivar, G. Cheng, M. Lopez, B. Kalyanaraman, Mitochondria-Targeted Triphenylphosphonium-Based Compounds: Syntheses, Mechanisms of Action, and Therapeutic and Diagnostic Applications, Chem Rev 117 (15) (2017) 10043–10120.
[25] S.D. Bernal, T.J. Lampidis, R.M. McIsaac, L.B. Chen, Anticarcinoma activity in vivo of rhodamine 123, a mitochondrial-specific dye, Science 222 (4620) (1983) 169–172.
[26] J.S. Modica-Napolitano, J.R. Aprille, Delocalized lipophilic cations selectively target the mitochondria of carcinoma cells, Advanced drug delivery reviews 49 (1–2) (2001) 63–70.
[27] J. Neuzil, L.F. Dong, J. Rohlena, J. Truksa, S.J. Ralph, Classification of mitocans, anti-cancer drugs acting on mitochondria, Mitochondrion 13 (3) (2013) 199–208.
[28] C.J. Barile, P.C. Herrmann, D.A. Tyvoll, J.P. Collman, R.A. Decreau, B.S. Bull, Inhibiting platelet-stimulated blood coagulation by inhibition of mitochondrial respiration, Proc Natl Acad Sci U S A 109 (7) (2012) 2539–2543.
[29] M. Tavallaie, R. Voshtani, X. Deng, Y. Qiao, F. Jiang, J.P. Collman, L. Fu, Moderation of mitochondrial respiration mitigates metabolic syndrome of aging, Proceedings of the National Academy of Sciences of the United States of America 117 (18) (2020) 9840–9850.
[30] Z. Wang, W. Guo, X. Kuang, S. Hou, H. Liu, Nanopreparations for mitochondria targeting drug delivery system: Current strategies and future prospective, Asian journal of pharmaceutical sciences 12 (6) (2017) 498–508.
[31] M. Karbowski, C. Kurono, M. Wozniak, M. Ostrowski, M. Teranishi, Y. Nishizawa, J. Usukura, T. Soji, T. Wakabayashi, Free radical-induced megamitochondria formation and apoptosis, Free Radic Biol Med 26 (3–4) (1999) 396–409.
[32] J. Dan Dunn, L.A. Alvarez, X. Zhang, T. Soldati, Reactive oxygen species and mitochondria: A nexus of cellular homeostasis, Redox Biol 6 (2015) 472–485.
[33] X.Q. Ye, Q. Li, G.H. Wang, F.F. Sun, G.J. Huang, X.W. Bian, S.C. Yu, G.S. Qian, Mitochondrial and energy metabolism-related properties as novel indicators of lung cancer stem cells, International journal of cancer 129 (4) (2011) 820–831.
[34] J. Jiang, S. Wu, L. Lv, X. Liu, L. Chen, X. Zhao, Q. Wang, Mitochondrial dysfunction, apoptosis and transcriptomic alterations induced by four strobilurins in zebrafish (Danio rerio) early life stages, Environmental pollution (Barking, Essex 253 (2019) (1987) 722–730.
[35] S. Elmore, Apoptosis: a review of programmed cell death, Toxicologic pathology 35 (4) (2007) 495–516.
[36] D. De Rasmo, A. Signorile, A. Santeramo, M. Larizza, P. Lattanzio, G. Capitanio, S. Papa, Intramitochondrial adenylyl cyclase controls the turnover of nuclear-encoded subunits and activity of mammalian complex I of the respiratory chain, Biochim Biophys Acta 1853 (1) (2015) 183–191.
[37] S. Kumar, S. Kostin, J.P. Flacke, H.P. Reusch, Y. Ladilov, Soluble adenylyl cyclase controls mitochondria-dependent apoptosis in coronary endothelial cells, J Biol Chem 284 (22) (2009) 14760–14768.
[38] T. Sun, Y.J. Xu, S.Y. Jiang, Z. Xu, B.Y. Cao, G. Sethi, Y.Y. Zeng, Y. Kong, X.L. Mao, Suppression of the USP10/CCND1 axis induces glioblastoma cell apoptosis, Acta pharmacologica Sinica (2020).
[39] H. Zhang, CCND1 silencing suppresses liver cancer stem cell differentiation through inhibiting autophagy, Human cell 33 (1) (2020) 140–147.
[40] L. Chang, R. Guo, Z. Yuan, H. Shi, D. Zhang, LncRNA HOTAIR Regulates CCND1 and CCND2 Expression by Sponging miR-206 in Ovarian Cancer, Cellular physiology and biochemistry : international journal of experimental cellular physiology, biochemistry, and pharmacology 49 (4) (2018) 1289–1303.
[41] S. Zhao, L. Kurenbekova, Y. Gao, A. Roos, C.J. Creighton, P. Rao, J. Hicks, T. K. Man, C. Lau, A.M. Brown, S.N. Jones, A.J. Lazar, D. Ingram, D. Lev, L. A. Donehower, J.T. Yustein, NKD2, a negative regulator of Wnt signaling, suppresses tumor growth and metastasis in osteosarcoma, Oncogene 34 (39) (2015) 5069–5079.
[42] R.D. Cardiff, C.H. Miller, R.J. Munn, Manual hematoxylin and eosin staining of mouse tissue sections, Cold Spring Harbor protocols 2014 (6) (2014) 655–658.